HHS Public Access

Author manuscript

Sci Transl Med. Author manuscript; available in PMC 2019 August 01.

Published in final edited form as:

Sci Transl Med. 2018 August 01; 10(452): . doi:10.1126/scitranslmed.aao5726.

Intravital microscopy of osteolytic progression and therapy response of cancer lesions in bone

Eleonora Dondossola[1], **Stephanie Alexander**[1,†], **Boris M. Holzapfel**[2,3], **Stefano Filippini**[1], **Michael W. Starbuck**[1], **Robert M. Hoffman**[4], **Nora Navone**[1], **Elena M. De-Juan-Pardo**[2], **Christopher J. Logothetis**[1], **Dietmar W. Hutmacher**[2,5], and **Peter Friedl**[1,6,7,*]

[1]David H. Koch Center for Applied Research of Genitourinary Cancers, The University of Texas MD Anderson Cancer Center, 1515 Holcombe Blvd, Houston, TX, 77030, USA [2]Centre in Regenerative Medicine, Institute of Health and Biomedical Innovation, Queensland University of Technology (QUT), 60 Musk Avenue, Kelvin Grove, QLD 4059 Brisbane, Australia [3]Orthopaedic Center for Musculoskeletal Research, University of Würzburg, Brettreichstr. 11, 97074 Würzburg, Germany [4]Department of Surgery, UC San Diego and AntiCancer, Inc., 7917 Ostrow Street, San Diego, CA 92111, USA [5]ARC Centre in Additive Biomanufacturing, Queensland University of Technology (QUT), 60 Musk Avenue, Kelvin Grove, QLD 4059, Brisbane, Australia [6]Radboud University Nijmegen, Nijmegen, The Netherlands [7]Cancer Genomics Centre (CGC.nl), 3584 Utrecht, The Netherlands

Abstract

Intravital multiphoton microscopy (iMPM) in mice provides access to cellular and molecular mechanisms of metastatic progression of cancers and the underlying interactions with the tumor stroma. Whereas iMPM of malignant disease has been performed for soft tissues, non-invasive iMPM of solid tumor in bone is lacking. Here, we combined miniaturized tissue-engineered bone constructs in nude mice with a skin window to non-invasively and repetitively monitor prostate cancer lesions by three-dimensional iMPM. In vivo ossicles developed large central cavities containing mature bone marrow surrounded by a thin cortex, and enabled tumor implantation and longitudinal iMPM over weeks. Tumors grew inside the bone cavity and along the cortical bone interface and induced niches of osteoclast activation (focal osteolysis). Interventional bisphosphonate therapy reduced osteoclast kinetics and osteolysis without perturbing tumor growth, indicating dissociation of the tumor-stroma axis. The ossicle window, with its high cavity-to-cortex ratio and long-term functionality, thus allows for the mechanistic dissection of reciprocal epithelial tumor/bone interactions and therapy response.

[*]Corresponding author. pfriedl@mdanderson.org; peter.friedl@radboudumc.nl.
[†]Present address: European Molecular Biology Laboratory, Cell Biology & Biophysics Unit, 69117, Heidelberg, Germany

Author Contributions: E.D., S. A., B. M. H., N.N., C.J.L., D.W.H. and P.F. designed research; R.M.H., E.M.D.J.P and D.W.H. provided materials; E.D., S.A., B.M.H., S.F., E.M.D.J.P and D.W.H. performed bone generation experiments; E.D., S.A., S.F performed iMPM experiments; E.D., S.F performed ex vivo MPM experiments and μCT; E.D. performed bone marrow transplant experiments and functional analysis of mTEBC; M.W.S performed TRAP staining and bone histomorphometry; E.D., S.A., S.F., M.W.S., D.W.H. and P.F. analyzed data; E.D. and P.F. wrote the paper; all authors read and corrected the manuscript.

Competing Interests: the authors do not have competing financial interest to declare.

Data and materials availability. The authors declare that all the relevant data supporting the findings of this study are available within the paper and its supplementary information, and from the corresponding authors upon reasonable request.

One-sentence summary:

A skin window enables non-invasive, longitudinal monitoring of cancer growth and therapy response in tissue-engineered bone in mice.

INTRODUCTION

Bone metastases account for many complications experienced by patients suffering from advanced stages of different cancers, such as prostate, breast and other epithelial tissues, with generally incurable outcomes (1, 2). After seeding in bone, cancer cells interact with the microenvironment and undergo molecular reprogramming, which supports both tumor growth and bone remodelling in a vicious cycle (3). To date, analysis of bone metastasis of solid tumors is mostly obtained by molecular approaches combined with histology and immunohistochemistry ex vivo, on fixed tissue material, and macroscopic imaging studies (1). Despite moving the field forward, these strategies lack the sensitivity to characterize dynamic and reciprocal interactions between malignant cells and the bone stroma during progression and therapy response, and the three-dimensional (3D) adaptive niches which provide this cross-talk. Thus, strategies for longitudinal monitoring of the tumor/stroma interface in bone are much needed to dissect the pathophysiology of bone metastasis and mechanisms of therapy outcome in both pre-clinical research and mechanistic studies accompanying clinical interventions (1).

3D and time-resolved analysis of the kinetics of tumor-stroma interactions at the single cell level have been performed by multi-parametric intravital multiphoton microscopy (iMPM) in small animals, using higher harmonic light scattering and near-infrared and infrared fluorescence excitation (4, 5). In soft tissues, optical access to primary or secondary tumors is achieved by innovative window systems (4, 6–10); however iMPM in mature bone is limited by poor optical accessibility due to its cortical thickness, which causes light scatter, and is further complicated by the complex topology of bone and multifocal organization of bone metastases (11–16). In the mouse calvaria, iMPM enables effective monitoring of osteoclasts and osteoblasts, hematopoietic stem cell functions (11–14) and their interaction with hematopoietic tumors (12, 17). However, calvarial bone lacks the cavity space for direct implantation and growth of solid tumor lesions. To visualize cells in the tibia, iMPM requires the surgical removal of both muscle and cortical bone for retrieving the kinetics of hematopoietic progenitor and myeloma cells, mostly as a one-time procedure (15, 16, 18). Due to its invasive nature and reduced imaging and mechanical stability (hence fracture risk), the tibia window has not been exploited for 3D longitudinal monitoring of the complex topology and slow progression kinetics of bone metastasis.

Tissue engineering allows for the generation of a shape-defined, morphologically, and functionally intact mature bone organ within the mouse skin to dissect mechanisms of cancer metastasis to bone, including breast and prostate cancer (19–23). Here, we combined a miniaturized tissue-engineered bone construct (mTEBC) with an optical skin window (10, 24) to create an ossicle with high optical accessibility for non-invasive time- and space-resolved long-term iMPM of tumor-stroma interactions, osteolytic bone remodeling, and the reprogramming of the bone microenvironment during experimental therapy in mice.

RESULTS

Miniaturized tissue engineered bone construct generation

To enable microscopic, non-destructive monitoring of both solid tumors and the bone microenvironment, a sufficiently large volume of the bone cavity must coincide with optically favorable bone anatomy, supporting tumor cell implantation and expansion and high optical accessibility. To achieve these requirements, we miniaturized medical-grade polycaprolactone (mPCL) scaffolds with an interconnected honeycomb pore network, functionalized with calcium phosphate (CaP) (Fig. 1A, B), as square micro-scaffolds (5 × 5 × 0.2 mm) (19–21) which were implanted into the dorsolateral flank of nude mice, underneath the future position of the skin imaging window (Fig. 1C). To induce ectopic bone formation, mPCL-CaP scaffolds were co-implanted with fibrin glue and recombinant human bone morphogenetic protein 7 (BMP7), which created an ectopic ellipsoidal bone within 30 days (Fig. 1D). The volume of the bone increased with the amount of co-administered BMP7, reaching 30 mm^3 with a relatively flat outer cortical bone surface parallel to the body surface (fig. S1), which represented an ideal geometry for juxtaposing an imaging window.

The generation of the miniaturized tissue engineered bone construct (mTEBC) occurred as a tri-phasic process. Initial bone deposition was associated with high osteoclast density and multiple sites of bone erosion, forming an incipient interosseous cavity with primordial cellular content (Fig. 1E, I; S2A-C). Until day 20, bone remodeling and maturation of the bone marrow led to a continuous cortical bone surrounding a well-defined cavity interspersed with trabecular bone, hematopoietic bone marrow, and bone stroma, including adipocytes, osteoclasts, osteoblasts and osteocytes (Fig 1F, I; S2A-C). By day 30, an ossicle with cortical bone of even surface geometry and consistent thickness, trabecular bone and niches of bone marrow was formed, which remained morphologically stable until up to 300 days (Fig 1G-I; S2A-D). In summary, a miniaturized bone organ that stably persists over months in the mouse skin was developed.

Minimal cortical thickness and maximal bone marrow cavity with mature marrow and vasculature

Cortical bone thickness critically confounds the optical resolution of cells located in the bone cavity (15, 25). We thus quantified the evolution of the cortical bone layer by second harmonic generation (SHG) microscopy, which detects collagenous bone matrix (Fig. 2A) (26). During development, the average thickness varied between 50 and 80 μm and uniformly stabilized at 53.3 ± 3.3 μm after 30 days (Fig. 2A, B). This thickness was validated by stereomicroscopy of native cross-sectioned bone (Fig. 2B, C). Despite attenuation of laser light by the bone (75% of power loss at the inner interface), this thickness enabled full-penetrance iMPM microscopy (Fig. 2D). In practice, we compensated light attenuation by z-power adaptation and reached ~2-fold improved excitation underneath the bone (Fig. 2E). Besides thickness, the quality of cortical bone improved over time as quantified by measuring the area of the micro-cavities decorating the bone surface (Fig. 2A, F). The geometry of micro-ossicles further offered a superior cavity (cross section 17–27 mm^2) and ratio to cortical thickness when compared to natural bones, including the mouse tibia, vertebra and rib, which are typical locations of prostate cancer (PCa) metastases, or the

calvaria, which is the most accessible location for iMPM of hematological neoplasias (Fig. 2G, H) (15, 25).

We next verified the physiological composition and functionality of the bone marrow in the engineered bone. The proportions of platelets, red and white cells, and the population distributions of granulocytes ($CD11b^+GR1^+$ cells), monocytes ($CD11b^+GR1^-$ cells) and B cells ($B220^+$ cells) present in the engineered bone were similar to the bone marrow isolated from tibia (fig. S3A-D). Furthermore, bone marrow transplantation using donor cells isolated from mTEBCs 40 days after implantation successfully reconstituted the bone marrow in lethally irradiated recipients (fig. S3E-G). Thus, similar to existing strategies to supplement bone-free hydrogels with type I collagen and bone marrow stromal cells (24) and large TEBCs functionalized with mesenchymal stem cells and BMP7 and BMP2 (20, 23), this miniaturized TBEC recreates a functional environment to recruit precursor cells and establish mature bone marrow (20, 23, 24).

The vasculature within the mTEBC consisted of perfused blood vessels detected by intravital microscopy after intravenous injection of AlexaFluor750 Dextran (70 kDa) (Fig. 2I; fig. S3A) and expressing the surface marker endomucin (fig. S3B), confirming vascular network organization and sinusoidal differentiation typical of natural bone (27). The vessel density present in the mTEBC showed a space occupancy of ~30% (Fig. 2I; fig. S3C), which matched the vascular density of natural bones used for intravital imaging in other contexts, including tibia and calvaria, and the mouse femur (28). In aggregate, the mTEBC develops a large bone cavity that harbors mature bone marrow and sinusoidal blood vessels and, due to the thin, optically-transparent cortex, presents a suitable geometry for monitoring solid bone tumor biology by iMPM.

Longitudinal intravital microscopy of solid tumors in bone

Preclinical analyses of therapy response require sufficiently consistent and metronomic cohort behavior. Spontaneous bone colonization from orthotopically implanted tumors or by cancer cells administered in the circulation recapitulate naturally occurring bone metastases, however these routes display low penetrance of macrometastases and high inter-individual variability (29). Thus, we applied PCa cells by direct injection into the ossicle. This route maximizes the comparability of tumor growth and therapy response between mice. It further minimizes metastatic dissemination to other organs, which increases the risk of premature euthanasia due to systemic tumor burden and compromises reliable therapy response monitoring.

To generate solid tumors in bone, we implanted 150,000 human osteolytic PC3 or osteoblastic C4–2B PCa cells as a dense cell suspension in ~3 μl of phosphate-buffered saline into the ossicle using a microneedle (Fig. 3A). PCa lesions within the mTEBC recapitulated the histo-topology of patient biopsies (Fig. 3B; fig. S4, S5A). To allow iMPM, a skin window was surgically applied to the mouse two weeks after tumor implantation without disrupting the outer cortex and the periosteum of the mTEBC (Fig. 3A). Using combined near-infrared and infrared iMPM through the intact cortical bone, PC3 lesions expressing H2B/eGFP and DsRed2 (30) signals were detected with subcellular resolution, revealing cell shape and nuclear states (including mitosis, apoptosis and interphase), as well

as the bone structure using SHG microscopy (Fig. 3C, D). The penetration depth reached typically up to 200 μm (4–6 cell layers) into compact-shaped, bulky tumor lesions (Fig. 3C, movie S1). Similar microscopic penetration depth and resolution were reached for C4–2B osteoblastic PCa tumors expressing H2B/mCherry and LifeAct/GFP, which detects F-actin (fig. S5D-E). Through the intact cortical bone, differential actin organization along cell-cell junctions and in subcellular protrusions was detected with subcellular detail (fig. S5E), indicating efficient monitoring of subcortical tumors in osteolytic and non-osteolytic tumor types. Tumor growth and suitability for iMPM were further confirmed using breast cancer cells (MDA-MB-231), which are known to metastasize to bone and induce osteolysis (fig. S5F-I) (31).

As in natural bone and large TEBCs, PC3 tumors caused macroscopic and microscopic osteolysis (21, 32), with focal osteoclast recruitment and erosion of the mineralized matrix (Fig. 4A), followed by progressing cortical bone defects that fused and ultimately led to near-complete dissolution of the mTEBC by day 34 (Fig. 4B; fig. S6). As a consequence of cortical bone erosion, improved imaging penetration depth in osteolytic lesions was achieved (Fig 4C versus 3C).

As a direct proxy for co-registering osteolytic activity along the tumor/bone interface by iMPM, remodeled bone was identified by fluorescent pamidronate (OsteoSense; OS) and osteoclasts were visualized by a cathepsin K sensor (Cat K; Fig. 4C) (33, 34). Cat K is a cysteine protease predominantly localized in the cytoplasm and endosomal/lysosomal compartments of osteoclasts (35). The 3D topology analysis of OS, Cat K, SHG and dual color PC3 cells was used to map zones of the tumor/bone interface, where nodular PC3 lesions were bordered by complex-shaped Cat K^+ phagocytes and osteoclasts (Fig. 4C, D; fig. S7; movie S2). The density of osteoclasts, detected by TRAP-staining in tissue sections or fluorescent Cat K probe in vivo, decreased with distance from the tumors (fig. S8), suggesting that solid PC3 tumors recruited Cat K-positive cells locally.

To map the dynamics of Cat K-positive cells along the zone of bone resorption, we performed time-lapse recordings to track the cell positions followed by particle image velocimetry for subcellular dynamics (movie S3). Osteoclasts in lacuna-like bone resorption niches, detected by SHG (fig. S6), remained positionally stable (Fig. 4E) but retained vigorous cytoplasmic and vesicle dynamics with variable speed up to 1.2 μm/min (Fig. 4F, G). Similar positional stability of bone-resorptive osteoclasts was reported for cancer-free calvarial bone (14). The general lack of protrusive activity of bulky PC3 lesions growing adjacent to osteolytic phagocytes/osteoclasts suggests that bone destruction occurs without signs of active tumor invasion.

Disconnecting the tumor/stroma interface by bisphosphonate treatment

To demonstrate the suitability of iMPM for longitudinal monitoring of therapy responses in the micro-ossicle, established PC3 lesions with incipient osteolysis were monitored sequentially during treatment with zoledronic acid (ZA) (Fig. 5A). ZA inhibits osteoclast-mediated bone resorption by modifying prenylation of proteins, including regulators of the cytoskeleton and vesicle trafficking involved in bone remodeling (36, 37). When given therapeutically to patients with metastatic cancer, ZA reduces bone pain and delays skeletal

degeneration (38). In control mice receiving vehicle, osteolysis progressed over time, with local resorption speeds of hundreds of μm/day when monitored by serial iMPM (Fig. 5B, C). As expected, ZA near-instantaneously and completely halted bone resorption at the macroscopic level (Fig. 5B, C). However, when monitored microscopically, residual dynamics of the bone interface in ZA-treated mice revealed ongoing focal micro-remodeling (Fig. 5D), with sub-regions of the same lesion progressing at 3 to 10 μm/day (Fig. 5E, F). ZA administration did not alter the density of Cat K^+ cells within 6 days of treatment (Fig. 5G), consistent with stable osteoclast density in clinical bone specimens (39, 40). However, particle image velocimetry of time-lapse recordings revealed that the subcellular kinetics of Cat K-positive cells was significantly decreased, resulting in both cell stasis and ablation of fast subcellular movements (Fig. 5H-J; fig. S9; movie S4 versus S5). ZA caused no change to PC3 cell growth, detected as the frequency of apoptotic and mitotic cells at the tumor-bone interface in the same lesions over time (Fig. 5K). This reveals that the primary effect of this bone-stabilizing therapy acts on the stromal but not tumor compartments.

DISCUSSION

Combining a tissue-engineered mature micro-ossicle with skin window-based intravital multiphoton microscopy provides a new strategy for longitudinal analysis of solid tumor interactions with bone, including tumor-induced osteolysis and therapy response. The uniformly thin cortex of the ossicle surrounds a large bone marrow cavity and permits both tumor implantation and iMPM through the intact bone lamella without perturbing bone integrity. Implanting a cell-free, CaP-functionalized scaffold in combination with BMP7 was sufficient to induce ossicle maturation followed by long-term stability for several hundred days. This indicates that BMP7, added during implantation, orchestrated neo-bone generation of the host tissue, in contrast to other mesenchymal stem-cell based strategies that depend on cell-based functionalization (41, 42).

Beside the reliably thin cortical lamella, key features of the miniaturized TEBC include (i) tailored, roundish shape optimal for juxtaposing with the imaging window; (ii) recruitment and maintenance of a mature bone marrow and vascular networks; and (iii) a reactive bone response to tumor growth, including osteoclast activation and bone erosion. These characteristics differ from other systems aimed at monitoring bone biology in vivo, including implanted bone fragments (43–45). Implanted bone fragments lack optical transparency and incompletely recreate vital bone, since over time they fail to support active bone neo-apposition, microvascularization development and recruitment of hematopoietic bone marrow precursor cells but instead frequently develop fibrosis (43–45). Thus, the mTEBC window model combines mature bone topology and functionality with accessibility for longitudinal intravital microscopy of tumors growing inside the bone cavity.

By positioning the skin window near the intact cortical bone, repeated 3D microscopy could resolve the position and activity of individual malignant and non-malignant cells inside the mTEBC, their subcellular kinetics (including mitosis, apoptosis and shape oscillations), and the spatial evolution of bone remodeling. During bone resorption, Cat K^+ cells accumulate at the tumor-bone interface, become largely stationary but retain vigorous subcellular dynamics and establish local resorption niches, which coalesce until the bone is destroyed, similar to

resorbing osteoclasts in vitro and in cancer-free calvaria in vivo (14, 46, 47). In vitro positional stability of osteoclasts is mediated by the podosome-rich sealing zone that focuses the lytic region to the bone surface and defines the bone resorption niche (46, 47). Concurrently, osteoclasts maintain highly dynamic substructures, including the actin-rich ruffle border engaged in Cat K release and resorption, lamellipodia exploring free bone surface (48–50), and Cat K-containing secretory vesicles, which depend upon the joint activity of the small GTPases Rac and Rab (37, 49). ZA inhibits the farnesyl diphosphate synthase and thereby prevents prenylation of small GTPases, including Rac and Rab, which inhibits their membrane localization and function (37). Consistently, ZA perturbs vesicular trafficking and essential actin structures in vitro, including the sealing zone, ruffling border and lamellipodia dynamics, and this combined effect likely impairs bone resorption (36, 37, 51). The in vivo effects of ZA on osteoclast dynamics and function, including impaired subcellular dynamics and near-ablated bone resorption, thus validate actin and vesicular dynamics as central effectors of bone remodeling. Importantly, ZA did not affect tumor cell viability and growth in vivo, which explains the clinically observed disconnect between the well-documented stabilization of bone despite unperturbed growth of the cancer lesions (52, 53) and clinical disease progression (54).

The conundrum between ZA-induced bone stabilization despite ongoing tumor growth further validates the use of the mTEBC model in support of bone remodeling as a secondary, largely osteoclast-dependent pathology, which can be uncoupled from tumor expansion. Beyond cancer, the ossicle window represents an anatomically stable and genetically versatile platform to enable a range of kinetic studies in basic bone biology, tissue engineering, and reparative medicine. Variation of the mTEBC will provide additional options for including human cells, such as hematopoietic stem cells or engineered stromal cells (mesenchymal stem cells/osteoblasts, osteoclasts or vascular cells), and genetic modulation of the bone stroma (20). Non-invasive monitoring of the tumor-bone interface may deliver preclinical and co-clinical insights into metastatic cancer progression, bone remodeling, and multi-targeted therapy response.

MATERIALS AND METHODS

Study design

The objective of this study was to establish a preclinical model for intravital microscopy of solid cancer in bone. Tissue engineering was applied to generate an ossicle that combines (i) minimal cortical thickness; (ii) large bone marrow cavity; (iii) mature bone marrow and vasculature; (iv) positioning in the skin suitable for applying an imaging window; and that (v) provides sufficient optical transparency for detecting cells with subcellular resolution by multiphoton microscopy through the intact cortical bone. Fluorescent microtumors were implanted directly and intra-bone tumor growth and osteolysis dynamics were three-dimensionally reconstructed by multi-channel intravital microscopy, and further monitored by bone histomorphometry, flow cytometry of maturity of the bone marrow and μCT for ossification. Using molecular reporters, the osteolytic tumor-bone interface was detected by intravital microscopy in the live mouse over time, including the composition and kinetics of collagen and bone matrix turnover (SHG), calcified bone (fluorescent bisphosphonates),

osteoclasts (cathepsin K) and cancer cells (nuclear and cytoplasmic fluorescent reporters). As a proof of concept the ossicle model was applied for intravital MPM of bisphosphonate therapy to halt bone remodeling and the effects on bone resorption, osteoclast and tumor biology recorded. Repeated microscopy of the same mouse allowed to obtain multiparametric longitudinal data from the same tumor, thereby maximizing data reliability and minimizing animal consumption. Accordingly, 3–5 mice per group were sufficient to reach statistical significance. Image acquisition in vivo and ex vivo from control and treated mice was performed in a blinded manner. Data analysis was performed in a non-blinded manner.

mTEBC generation, tumor cell injection, and dorsal skinfold chamber (DSFC) creation.

Animal studies were approved by the Institutional Animal Care and Use Committee of The University of Texas, MD Anderson Cancer Center and performed according to the institutional guidelines for animal care and handling. To generate a micro-ossicle, male and female nu/nu athymic or male NOD-SCID mice, 4-weeks old (provided by the Dept. of Experimental Radiation Oncology, MD Anderson Cancer Center) were anesthetized using ketamine/xylazine and a 5 × 5 × 0.2 mm (length x width x thickness) mPCL-CaP scaffold was inserted into a small surgical subcutaneous pocket (4–5 mm) in the presence of fibrin glue (5 μl fibrinogen/5 μl thrombin; Fibrin Sealant Tisseel, Baxter) and 10 μl of BMP7 (10 mg/ml, Gibco) followed by wound closure (1 or 2 4.0 polypropylene sutures, Covidien). The subdermal implantation site preserved the integrity of the muscular tissue and fasciae of the underlying ribs and spines. Ossicle formation was independent of implantation site in different locations in the back of the mouse. At least 30 days post-surgery, tumor cells (1.5×10^5 cells in 3–5 μl of phosphate-buffered saline, PBS) were injected into the mTEBC (30G x ½ needle), as follows: PC3 cells in male nu/nu athymic mice, C4–2B cells in male NOD-SCID mice and MDA-MB-231 cells in female nu/nu athymic mice. When the lesion was identifiable by epifluorescence microscopy (10–14 days after implantation), a titanium dorsal skin-fold chamber with a glass window (diameter 11.5 mm; Machine Shop, University Clinics Munich, Grosshadern, Munich) was mounted adjacent to the tumor cell-bearing organ bone. The mTEBC was centered in the window system and subcutaneous tissue deposited on the bone was carefully removed, avoiding any damage to afferent vessels as well as the periosteum, and the procedure continued as described elsewhere (9, 10).

Statistical analysis.

Statistical analysis was performed using GraphPad Prism 7.0a, as described in the figure legends. To test differences between two populations the unpaired two-tailed Student t-test was applied. To test the differences among more than two populations one-way ANOVA followed by Tukey's HSD post-hoc test was performed. Unless stated otherwise, data are shown as means ± SD.

Supplementary Material

Refer to Web version on PubMed Central for supplementary material.

Acknowledgments:

We thank Steve Alexander for maintenance and support with the multiphoton microscope; Carol Johnston for histological processing of the samples; Bettina Weigelin for endomucin stainings; Charles Kingsley, Kiersten Maldonado, Keith Michel and Jorge Delacerda for support with μCT application.

Funding: E.D. is supported by the Cancer Prevention and Research Institute of Texas (RP140482), TX, USA, the Prostate Cancer Foundation (16YOUN24), CA, USA and The Rolanette and Berdon Lawrence Bone Disease Program of Texas, TX, USA; P.F. is supported by NWO-VICI (918.11.626), the European Research Council (ERC-CoG DEEPINSIGHT, Project No. 617430), the NIH (U54 CA210184–01) and the Cancer Genomics Cancer, The Netherlands; D.W.H. is supported by the Australian Research Council Training Centre in Additive Biomanufacturing, the National Health and Medical Research Council of Australia, National Breast Cancer Foundation (IN-15–047) and World Cancer Foundation. The Genitourinary Cancers Program of the CCSG shared resources at MD Anderson Cancer Center was supported by NIH/NCI award number P30 CA016672. N.N. is supported by the University of Texas MD Anderson Moon Shots Program.

REFERENCES AND NOTES

1. Weilbaecher KN, Guise TA, McCauley LK, Cancer to bone: a fatal attraction. Nat Rev Cancer 11, 411–425 (2011); published online EpubJun (nrc30550.1038/nrc3055). [PubMed: 21593787]
2. Croucher PI, McDonald MM, Martin TJ, Bone metastasis: the importance of the neighbourhood. Nat Rev Cancer 16, 373–386 (2016); published online EpubMay 25 (10.1038/nrc.2016.44). [PubMed: 27220481]
3. Ell B, Kang Y, SnapShot: Bone Metastasis. Cell 151, 690–690 e691 (2012); published online EpubOct 26 (10.1016/j.cell.2012.10.005). [PubMed: 23101634]
4. Ellenbroek SI, van Rheenen J, Imaging hallmarks of cancer in living mice. Nat Rev Cancer 14, 406–418 (2014); published online EpubJun (10.1038/nrc3742). [PubMed: 24854083]
5. Andresen V, Alexander S, Heupel WM, Hirschberg M, Hoffman RM, Friedl P, Infrared multiphoton microscopy: subcellular-resolved deep tissue imaging. Current opinion in biotechnology 20, 54–62 (2009); published online EpubFeb (10.1016/j.copbio.2009.02.008). [PubMed: 19324541]
6. Kedrin D, Gligorijevic B, Wyckoff J, Verkhusha VV, Condeelis J, Segall JE, van Rheenen J, Intravital imaging of metastatic behavior through a mammary imaging window. Nature methods 5, 1019–1021 (2008); published online EpubDec (10.1038/nmeth.1269). [PubMed: 18997781]
7. Ritsma L, Steller EJ, Beerling E, Loomans CJ, Zomer A, Gerlach C, Vrisekoop N, Seinstra D, van Gurp L, Schafer R, Raats DA, de Graaff A, Schumacher TN, de Koning EJ, Rinkes IH, Kranenburg O, van Rheenen J, Intravital microscopy through an abdominal imaging window reveals a pre-micrometastasis stage during liver metastasis. Science translational medicine 4, 158ra145 (2012); published online EpubOct 31 (10.1126/scitranslmed.3004394).
8. Kienast Y, von Baumgarten L, Fuhrmann M, Klinkert WE, Goldbrunner R, Herms J, Winkler F, Real-time imaging reveals the single steps of brain metastasis formation. Nat Med 16, 116–122 (2010); published online EpubJan (10.1038/nm.2072). [PubMed: 20023634]
9. Guba M, von Breitenbuch P, Steinbauer M, Koehl G, Flegel S, Hornung M, Bruns CJ, Zuelke C, Farkas S, Anthuber M, Jauch KW, Geissler EK, Rapamycin inhibits primary and metastatic tumor growth by antiangiogenesis: involvement of vascular endothelial growth factor. Nat Med 8, 128–135 (2002); published online EpubFeb (10.1038/nm0202–128). [PubMed: 11821896]
10. Alexander S, Koehl GE, Hirschberg M, Geissler EK, Friedl P, Dynamic imaging of cancer growth and invasion: a modified skin-fold chamber model. Histochemistry and cell biology 130, 1147–1154 (2008); published online EpubDec (10.1007/s00418–008-0529–1). [PubMed: 18987875]
11. Lo Celso C, Fleming HE, Wu JW, Zhao CX, Miake-Lye S, Fujisaki J, Cote D, Rowe DW, Lin CP, Scadden DT, Live-animal tracking of individual haematopoietic stem/progenitor cells in their niche. Nature 457, 92–96 (2009); published online EpubJan 1 (10.1038/nature07434). [PubMed: 19052546]
12. Sipkins DA, Wei X, Wu JW, Runnels JM, Cote D, Means TK, Luster AD, Scadden DT, Lin CP, In vivo imaging of specialized bone marrow endothelial microdomains for tumour engraftment. Nature 435, 969–973 (2005); published online EpubJun 16 (nature03703 [pii] 10.1038/nature03703). [PubMed: 15959517]

13. Park D, Spencer JA, Koh BI, Kobayashi T, Fujisaki J, Clemens TL, Lin CP, Kronenberg HM, Scadden DT, Endogenous bone marrow MSCs are dynamic, fate-restricted participants in bone maintenance and regeneration. Cell Stem Cell 10, 259–272 (2012); published online EpubMar 2 (10.1016/j.stem.2012.02.003). [PubMed: 22385654]

14. Kikuta J, Wada Y, Kowada T, Wang Z, Sun-Wada GH, Nishiyama I, Mizukami S, Maiya N, Yasuda H, Kumanogoh A, Kikuchi K, Germain RN, Ishii M, Dynamic visualization of RANKL and Th17-mediated osteoclast function. J Clin Invest 123, 866–873 (2013); published online EpubFeb (10.1172/JCI65054). [PubMed: 23321670]

15. Kohler A, Schmithorst V, Filippi MD, Ryan MA, Daria D, Gunzer M, Geiger H, Altered cellular dynamics and endosteal location of aged early hematopoietic progenitor cells revealed by time-lapse intravital imaging in long bones. Blood 114, 290–298 (2009); published online EpubJul 9 (10.1182/blood-2008–12-195644). [PubMed: 19357397]

16. Lawson MA, McDonald MM, Kovacic N, Hua Khoo W, Terry RL, Down J, Kaplan W, Paton-Hough J, Fellows C, Pettitt JA, Neil Dear T, Van Valckenborgh E, Baldock PA, Rogers MJ, Eaton CL, Vanderkerken K, Pettit AR, Quinn JM, Zannettino AC, Phan TG, Croucher PI, Osteoclasts control reactivation of dormant myeloma cells by remodelling the endosteal niche. Nat Commun 6, 8983 (2015)10.1038/ncomms9983). [PubMed: 26632274]

17. Hawkins ED, Duarte D, Akinduro O, Khorshed RA, Passaro D, Nowicka M, Straszkowski L, Scott MK, Rothery S, Ruivo N, Foster K, Waibel M, Johnstone RW, Harrison SJ, Westerman DA, Quach H, Gribben J, Robinson MD, Purton LE, Bonnet D, Lo Celso C, T-cell acute leukaemia exhibits dynamic interactions with bone marrow microenvironments. Nature 538, 518–522 (2016); published online EpubOct 27 (10.1038/nature19801). [PubMed: 27750279]

18. Kim S, Lin L, Brown GA, Hosaka K, Scott EW, Extended time-lapse in vivo imaging of tibia bone marrow to visualize dynamic hematopoietic stem cell engraftment. Leukemia, (2017); published online EpubJan 13 (10.1038/leu.2016.354).

19. Holzapfel BM, Hutmacher DW, Nowlan B, Barbier V, Thibaudeau L, Theodoropoulos C, Hooper JD, Loessner D, Clements JA, Russell PJ, Pettit AR, Winkler IG, Levesque JP, Tissue engineered humanized bone supports human hematopoiesis in vivo. Biomaterials 61, 103–114 (2015); published online EpubAug (10.1016/j.biomaterials.2015.04.057). [PubMed: 26001075]

20. Martine LC, Holzapfel BM, McGovern JA, Wagner F, Quent VM, Hesami P, Wunner FM, Vaquette C, De-Juan-Pardo EM, Brown TD, Nowlan B, Wu DJ, Hutmacher CO, Moi D, Oussenko T, Piccinini E, Zandstra PW, Mazzieri R, Levesque JP, Dalton PD, Taubenberger AV, Hutmacher DW, Engineering a humanized bone organ model in mice to study bone metastases. Nature protocols 12, 639–663 (2017); published online EpubApr (10.1038/nprot.2017.002). [PubMed: 28253234]

21. Holzapfel BM, Wagner F, Loessner D, Holzapfel NP, Thibaudeau L, Crawford R, Ling MT, Clements JA, Russell PJ, Hutmacher DW, Species-specific homing mechanisms of human prostate cancer metastasis in tissue engineered bone. Biomaterials 35, 4108–4115 (2014); published online EpubApr (10.1016/j.biomaterials.2014.01.062). [PubMed: 24534484]

22. Thibaudeau L, Taubenberger AV, Holzapfel BM, Quent VM, Fuehrmann T, Hesami P, Brown TD, Dalton PD, Power CA, Hollier BG, Hutmacher DW, A tissue-engineered humanized xenograft model of human breast cancer metastasis to bone. Disease models & mechanisms 7, 299–309 (2014); published online EpubFeb (10.1242/dmm.014076). [PubMed: 24713276]

23. Seib FP, Berry JE, Shiozawa Y, Taichman RS, Kaplan DL, Tissue engineering a surrogate niche for metastatic cancer cells. Biomaterials 51, 313–319 (2015); published online EpubMay (10.1016/j.biomaterials.2015.01.076). [PubMed: 25771021]

24. Lee J, Li M, Milwid J, Dunham J, Vinegoni C, Gorbatov R, Iwamoto Y, Wang F, Shen K, Hatfield K, Enger M, Shafiee S, McCormack E, Ebert BL, Weissleder R, Yarmush ML, Parekkadan B, Implantable microenvironments to attract hematopoietic stem/cancer cells. Proc Natl Acad Sci U S A 109, 19638–19643 (2012); published online EpubNov 27 (10.1073/pnas.1208384109). [PubMed: 23150542]

25. Lo Celso C, Lin CP, Scadden DT, In vivo imaging of transplanted hematopoietic stem and progenitor cells in mouse calvarium bone marrow. Nature protocols 6, 1–14 (2011); published online EpubJan (10.1038/nprot.2010.168). [PubMed: 21212779]

26. Weigelin B, Bakker GJ, Friedl P, Third harmonic generation microscopy of cells and tissue organization. J Cell Sci 129, 245–255 (2016); published online EpubJan 15 (10.1242/jcs.152272). [PubMed: 26743082]
27. Kusumbe AP, Ramasamy SK, Adams RH, Coupling of angiogenesis and osteogenesis by a specific vessel subtype in bone. Nature 507, 323–328 (2014); published online EpubMar 20 (10.1038/nature13145). [PubMed: 24646994]
28. Kunisaki Y, Bruns I, Scheiermann C, Ahmed J, Pinho S, Zhang D, Mizoguchi T, Wei Q, Lucas D, Ito K, Mar JC, Bergman A, Frenette PS, Arteriolar niches maintain haematopoietic stem cell quiescence. Nature 502, 637–643 (2013); published online EpubOct 31 (10.1038/nature12612). [PubMed: 24107994]
29. Singh AS, Figg WD, In vivo models of prostate cancer metastasis to bone. J Urol 174, 820–826 (2005); published online EpubSep (10.1097/01.ju.0000169133.82167.aa). [PubMed: 16093963]
30. Hoffman RM, The multiple uses of fluorescent proteins to visualize cancer in vivo. Nat Rev Cancer 5, 796–806 (2005); published online EpubOct (10.1038/nrc1717). [PubMed: 16195751]
31. Kang Y, Siegel PM, Shu W, Drobnjak M, Kakonen SM, Cordon-Cardo C, Guise TA, Massague J, A multigenic program mediating breast cancer metastasis to bone. Cancer Cell 3, 537–549 (2003); published online EpubJun ([PubMed: 12842083]
32. Simmons JK, Hildreth BE, 3rd, Supsavhad W, Elshafae SM, Hassan BB, Dirksen WP, Toribio RE, Rosol TJ, Animal Models of Bone Metastasis. Veterinary pathology 52, 827–841 (2015); published online EpubSep (10.1177/0300985815586223). [PubMed: 26021553]
33. Lassailly F, Foster K, Lopez-Onieva L, Currie E, Bonnet D, Multimodal imaging reveals structural and functional heterogeneity in different bone marrow compartments: functional implications on hematopoietic stem cells. Blood 122, 1730–1740 (2013); published online EpubSep 5 (10.1182/blood-2012–11-467498). [PubMed: 23814020]
34. Kozloff KM, Quinti L, Patntirapong S, Hauschka PV, Tung CH, Weissleder R, Mahmood U, Non-invasive optical detection of cathepsin K-mediated fluorescence reveals osteoclast activity in vitro and in vivo. Bone 44, 190–198 (2009); published online EpubFeb (10.1016/j.bone.2008.10.036). [PubMed: 19007918]
35. Turk V, Stoka V, Vasiljeva O, Renko M, Sun T, Turk B, Turk D, Cysteine cathepsins: from structure, function and regulation to new frontiers. Biochim Biophys Acta 1824, 68–88 (2012); published online EpubJan (10.1016/j.bbapap.2011.10.002). [PubMed: 22024571]
36. Rogers TL, Holen I, Tumour macrophages as potential targets of bisphosphonates. J Transl Med 9, 177 (2011)10.1186/1479-5876-9-177). [PubMed: 22005011]
37. Itzstein C, Coxon FP, Rogers MJ, The regulation of osteoclast function and bone resorption by small GTPases. Small GTPases 2, 117–130 (2011); published online EpubMay (10.4161/sgtp.2.3.16453). [PubMed: 21776413]
38. Lipton A, Bone loss prevention in cancer: new developments and perspectives. Seminars in oncology 37 Suppl 1, S1–2 (2010); published online EpubJun (10.1053/j.seminoncol.2010.06.005).
39. Weinstein RS, Roberson PK, Manolagas SC, Giant osteoclast formation and long-term oral bisphosphonate therapy. N Engl J Med 360, 53–62 (2009); published online EpubJan 1 (10.1056/NEJMoa0802633). [PubMed: 19118304]
40. Jobke B, Milovanovic P, Amling M, Busse B, Bisphosphonate-osteoclasts: changes in osteoclast morphology and function induced by antiresorptive nitrogen-containing bisphosphonate treatment in osteoporosis patients. Bone 59, 37–43 (2014); published online EpubFeb (10.1016/j.bone.2013.10.024). [PubMed: 24211427]
41. Antonelli A, Noort WA, Jaques J, de Boer B, de Jong-Korlaar R, Brouwers-Vos AZ, Lubbers-Aalders L, van Velzen JF, Bloem AC, Yuan H, de Bruijn JD, Ossenkoppele GJ, Martens AC, Vellenga E, Groen RW, Schuringa JJ, Establishing human leukemia xenograft mouse models by implanting human bone marrow-like scaffold-based niches. Blood 128, 2949–2959 (2016); published online EpubDec 22 (10.1182/blood-2016–05-719021). [PubMed: 27733356]
42. Chen Y, Jacamo R, Shi YX, Wang RY, Battula VL, Konoplev S, Strunk D, Hofmann NA, Reinisch A, Konopleva M, Andreeff M, Human extramedullary bone marrow in mice: a novel in vivo model

of genetically controlled hematopoietic microenvironment. Blood 119, 4971–4980 (2012); published online EpubMay 24 (10.1182/blood-2011–11-389957). [PubMed: 22490334]

43. Hubin F, Humblet C, Belaid Z, Greimers R, Boniver J, Thiry A, Defresne MP, Maintenance of functional human cancellous bone and human hematopoiesis in NOD/SCID mice. Cell Transplant 13, 823–831 (2004). [PubMed: 15690985]
44. Kuperwasser C, Dessain S, Bierbaum BE, Garnet D, Sperandio K, Gauvin GP, Naber SP, Weinberg RA, Rosenblatt M, A mouse model of human breast cancer metastasis to human bone. Cancer Res 65, 6130–6138 (2005); published online EpubJul 15 (10.1158/0008–5472.CAN-04–1408). [PubMed: 16024614]
45. Tassone P, Neri P, Kutok JL, Tournilhac O, Santos DD, Hatjiharissi E, Munshi V, Venuta S, Anderson KC, Treon SP, Munshi NC, A SCID-hu in vivo model of human Waldenstrom macroglobulinemia. Blood 106, 1341–1345 (2005); published online EpubAug 15 (10.1182/blood-2004–11-4477). [PubMed: 15886318]
46. Vaananen HK, Hentunen T, Lakkakorpi P, Parvinen EK, Sundqvist K, Tuukkanen J, Mechanism of osteoclast mediated bone resorption. Annales chirurgiae et gynaecologiae 77, 193–196 (1988). [PubMed: 3076045]
47. Anderegg F, Geblinger D, Horvath P, Charnley M, Textor M, Addadi L, Geiger B, Substrate adhesion regulates sealing zone architecture and dynamics in cultured osteoclasts. PLoS One 6, e28583 (2011)10.1371/journal.pone.0028583). [PubMed: 22162778]
48. Georgess D, Machuca-Gayet I, Blangy A, Jurdic P, Podosome organization drives osteoclast-mediated bone resorption. Cell adhesion & migration 8, 191–204 (2014). [PubMed: 24714644]
49. Sakai H, Chen Y, Itokawa T, Yu KP, Zhu ML, Insogna K, Activated c-Fms recruits Vav and Rac during CSF-1-induced cytoskeletal remodeling and spreading in osteoclasts. Bone 39, 1290–1301 (2006); published online EpubDec (10.1016/j.bone.2006.06.012). [PubMed: 16950670]
50. Destaing O, Saltel F, Geminard JC, Jurdic P, Bard F, Podosomes display actin turnover and dynamic self-organization in osteoclasts expressing actin-green fluorescent protein. Mol Biol Cell 14, 407–416 (2003); published online EpubFeb (10.1091/mbc.E02–07-0389). [PubMed: 12589043]
51. Rogers MJ, Crockett JC, Coxon FP, Monkkonen J, Biochemical and molecular mechanisms of action of bisphosphonates. Bone 49, 34–41 (2011); published online EpubJul (10.1016/j.bone.2010.11.008). [PubMed: 21111853]
52. Smith MR, Halabi S, Ryan CJ, Hussain A, Vogelzang N, Stadler W, Hauke RJ, Monk JP, Saylor P, Bhoopalam N, Saad F, Sanford B, Kelly WK, Morris M, Small EJ, Randomized controlled trial of early zoledronic acid in men with castration-sensitive prostate cancer and bone metastases: results of CALGB 90202 (alliance). J Clin Oncol 32, 1143–1150 (2014); published online EpubApr 10 (10.1200/JCO.2013.51.6500). [PubMed: 24590644]
53. Wirth M, Tammela T, Cicalese V, Gomez Veiga F, Delaere K, Miller K, Tubaro A, Schulze M, Debruyne F, Huland H, Patel A, Lecouvet F, Caris C, Witjes W, Prevention of bone metastases in patients with high-risk nonmetastatic prostate cancer treated with zoledronic acid: efficacy and safety results of the Zometa European Study (ZEUS). European urology 67, 482–491 (2015); published online EpubMar (10.1016/j.eururo.2014.02.014). [PubMed: 24630685]
54. Saad F, Gleason DM, Murray R, Tchekmedyian S, Venner P, Lacombe L, Chin JL, Vinholes JJ, Goas JA, Chen B, Zoledronic G Acid Prostate Cancer Study, A randomized, placebo-controlled trial of zoledronic acid in patients with hormone-refractory metastatic prostate carcinoma. J Natl Cancer Inst 94, 1458–1468 (2002); published online EpubOct 02 ([PubMed: 12359855]
55. Dondossola EH, Alexander BM, Filippini S, Hutmacher S, W. D; Friedl P, Examination of the foreign body response to biomaterials by nonlinear intravital microscopy. Nat. Biomed. Eng 1, (2016).
56. Schneider CA, Rasband WS, Eliceiri KW, NIH Image to ImageJ: 25 years of image analysis. Nature methods 9, 671–675 (2012); published online EpubJul ([PubMed: 22930834]
57. Dempster DW, Compston JE, Drezner MK, Glorieux FH, Kanis JA, Malluche H, Meunier PJ, Ott SM, Recker RR, Parfitt AM, Standardized nomenclature, symbols, and units for bone histomorphometry: a 2012 update of the report of the ASBMR Histomorphometry Nomenclature Committee. J Bone Miner Res 28, 2–17 (2013); published online EpubJan (10.1002/jbmr.1805). [PubMed: 23197339]

58. Fossey S, Vahle J, Long P, Schelling S, Ernst H, Boyce RW, Jolette J, Bolon B, Bendele A, Rinke M, Healy L, High W, Roth DR, Boyle M, Leininger J, Nonproliferative and Proliferative Lesions of the Rat and Mouse Skeletal Tissues (Bones, Joints, and Teeth). Journal of toxicologic pathology 29, 49S–103S (2016)10.1293/tox.29.3S-2). [PubMed: 27621538]

59. Acar M, Kocherlakota KS, Murphy MM, Peyer JG, Oguro H, Inra CN, Jaiyeola C, Zhao Z, Luby-Phelps K, Morrison SJ, Deep imaging of bone marrow shows non-dividing stem cells are mainly perisinusoidal. Nature 526, 126–130 (2015); published online EpubOct 1 (10.1038/nature15250). [PubMed: 26416744]

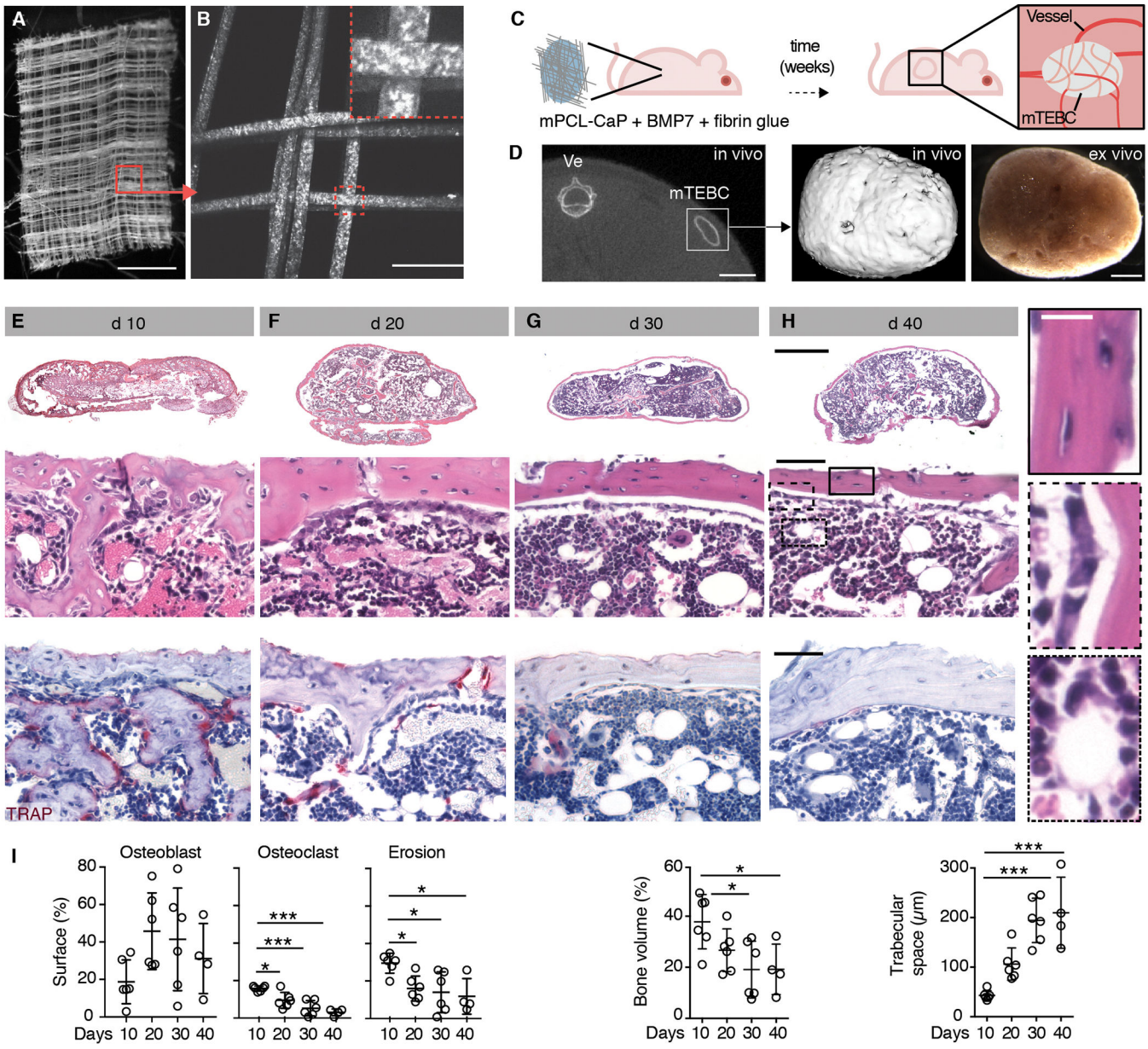

Fig. 1. Generation and characterization of a tissue-engineered ossicle in vivo.

(A) Macroscopic overview of melt electrospun mPCL-CaP scaffold by bright-field microscopy. Box, magnification shown in (**B**). Bar, 1 mm. **(B)** Maximum intensity projection of mPCL-CaP scaffold by multiphoton-excited second harmonic generation (SHG) detection (z-depth 100 μm). Box, magnification. Bar, 100 μm. (**C**) Schematic representation of the model. Nude mice were implanted subcutaneously with an mPCL-CaP scaffold embedded in fibrin glue and BMP7 (10 μg/mouse) that generated a mature, vascularized ossicle over time. (**D**) Localization of the ossicle (mTEBC) by μCT at day 30. Ve, vertebra; box, representative 3D reconstruction and bright field image shown on the right. Bars, 5 and 1 mm, respectively. (**E-H)** Histological overview, cortical detail and TRAP staining showing mTEBC maturation over time (**E**, d 10; **F**, d 20; **G**, d 30; **H**, d 40; d, day after implantation). Bars 1 mm

(overviews) and 100 μm (zooms). Insets show higher magnifications of boxed regions in (**H**). Bar, 25 μm. **(I)** Quantification by bone histomorphometry. Parameters analyzed: osteoblast surface (% of total bone surface; Ob. S/BS %); osteoclast surface (% of total bone surface; Oc. S/BS, %); erosion surface (% of total bone surface; ES/BS, %); bone volume (% of tissue volume; BV/TV, %); and trabecular separation (Tb. Sp.). Mean ± SD is shown, n=4–6/group. Bone cortex measurements, 5 cortical areas/mTEBC, 350 × 150 μm each; medullary region measurements, 4 areas/mTEBC, 250 × 250 μm each. *$P < 0.05$; *** $P < 0.001$ by one-way ANOVA followed by Tukey's HSD post-hoc test.

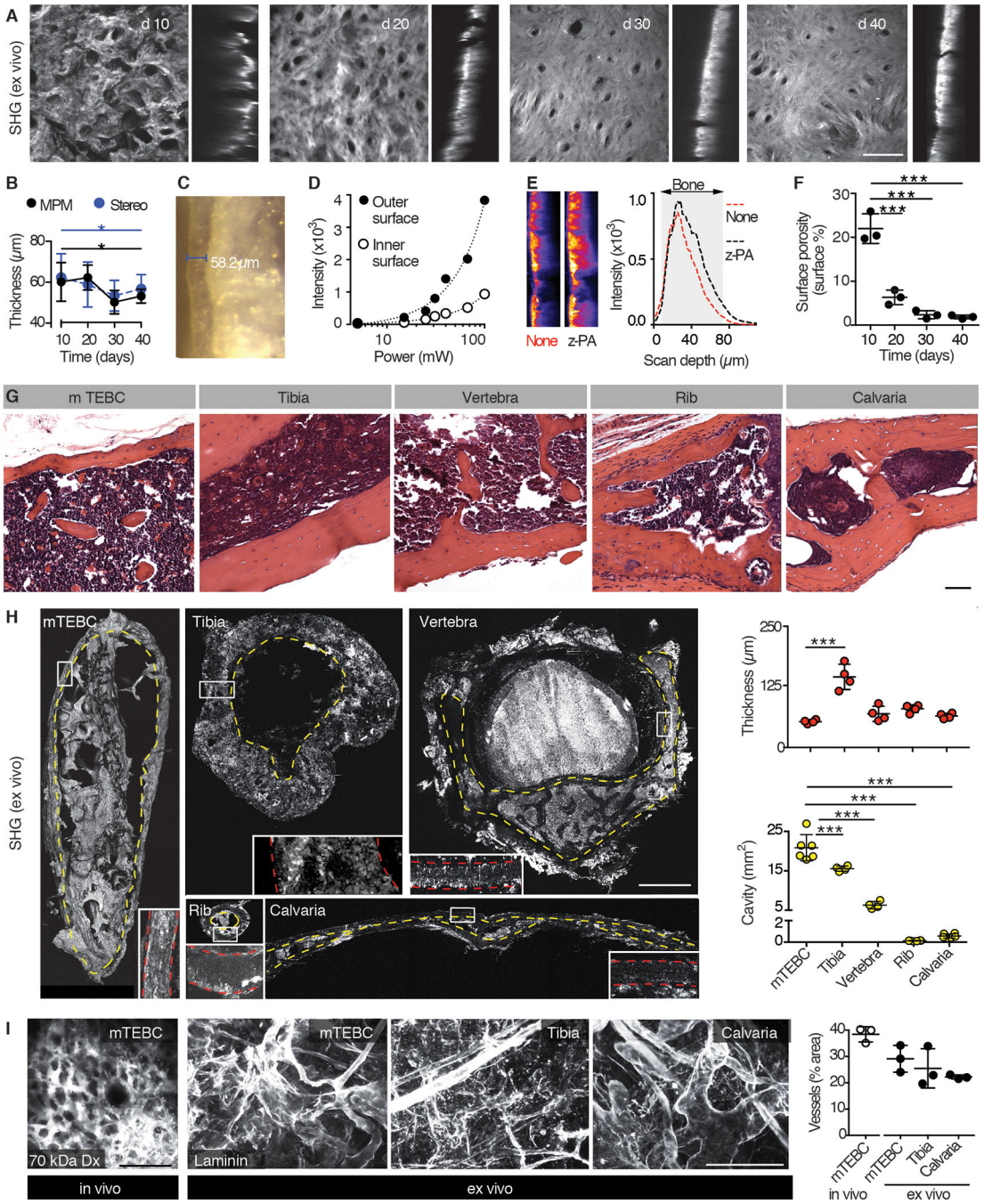

Fig. 2. Analysis of the mTEBC morphology.

(**A**) Maximum intensity projection of the SHG signal to detect the cortical bone of the ossicle ex vivo at days 10, 20, 30 and 40. Horizontal (xy, left) and orthogonal view (xz, right) are shown (z-depth, 150 μm). Bar, 100 μm. (**B, C**) Quantification of cortical bone thickness by MPM or stereomicroscope (image in **C**). Mean ± SD, 6 areas/mTEBC were averaged, 3 ossicles from independent mice per time point. (**D**) Measurement of the signal intensity in dependence of the laser power at the outer and inner cortical bone surface. Scanning wavelength, 1090 nm. One representative out of two independent experiment is

shown. (**E**) Z-power adaptation. Representative orthogonal view (xz) images of increased intensity and signal distribution are shown. Scanning wavelength, 1090 nm. (**F**) Quantification of surface porosity, represented as mean ± SD; individual data points are shown (6 areas/mTEBC were averaged, 3 ossicles from independent mouse per time point). (**G**) Histology (H&E) of the ossicle compared to the mouse tibia, vertebra, rib and calvaria. Bar, 50 μm. (**H).** 3D SHG reconstruction of the indicated bones (z-depth of specimen: TEBC, 1 mm; tibia, 800 μm; vertebra, 1 mm; rib, 400 μm; calvaria, 800 μm). Yellow dotted line, cavity. Box, magnification of cortical bone. Red dotted line, cortical bone. Data represent the mean ± SD, n=4–6 independent samples. (**I**) Left panel: intravital detection of blood vessels in the mTEBC (70 kDa AlexaFluor-750-conjugated Dextran, dx). Central and right panels: MPM detection of blood vessels (laminin) in cleared mTEBC, tibia, and calvaria ex vivo. Right panel: quantification (mean ± SD, n=3). Bar, 100 μm. $*P < 0.05$; $***P < 0.001$ by one-way ANOVA followed by Tukey's HSD post-hoc test.

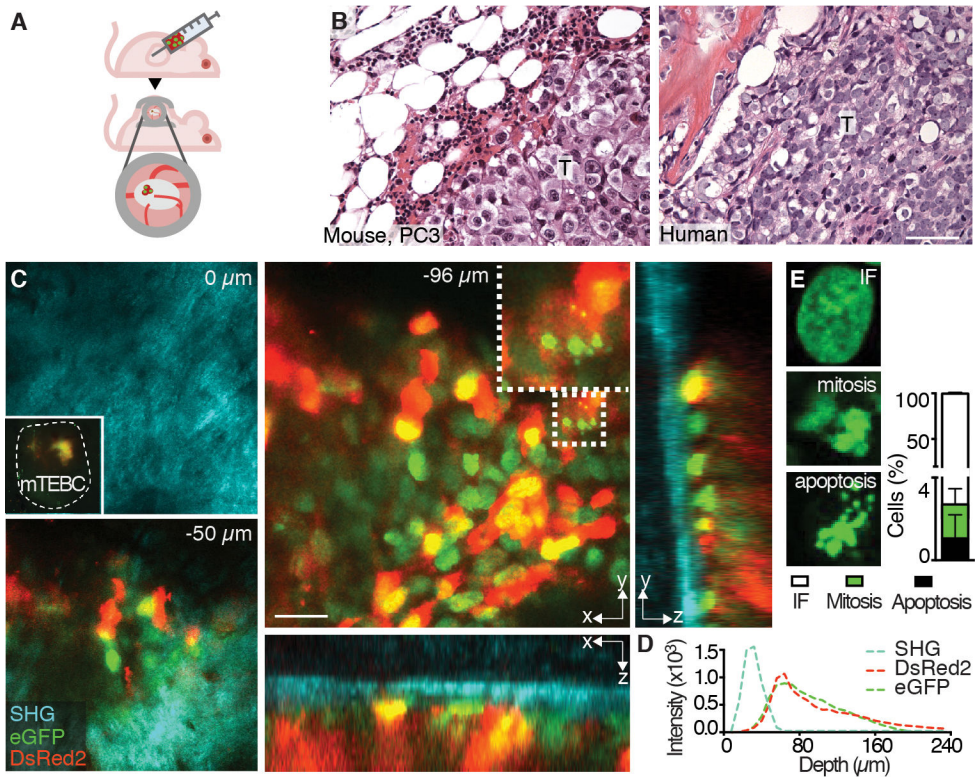

Fig. 3. PC3 tumor cell administration and monitoring by histology and iMPM.

(**A**) Schematic representation of the model. PC3 cells were injected into the mature ossicle 30 days after implantation into nude mice. A dorsal skin-fold chamber was applied 10–14 days post-tumor cell implantation, adjacent to the ossicle to enable iMPM. **(B)** Histology of PC3 cells in mTEBC and patient biopsy. T, tumor. Bar, 100 μm. **(C)** iMPM detection of PC3 cells at different scanning depths (z-stack at z=0, −50 and −96 μm). Overviews shown as xy and xz, yz orthogonal sections and detail with subcellular resolution (dotted box). Dashed line in top left panel denoted the edge of the ossicle with fluorescence signal originating from the tumor. **(D)** Xz intensity profile of individual channels with increasing scanning depth into the ossicle. **(E)** Quantification of interphase (IF), mitotic, or apoptotic cells in 3D stacks captured by iMPM. Mean ± SD is shown, n=5 independent lesions. Nucleus = H2B/eGFP, green; cytoplasm = DsRed2, red; collagen fibers, bone = SHG, cyan. Bar, 100 μm.

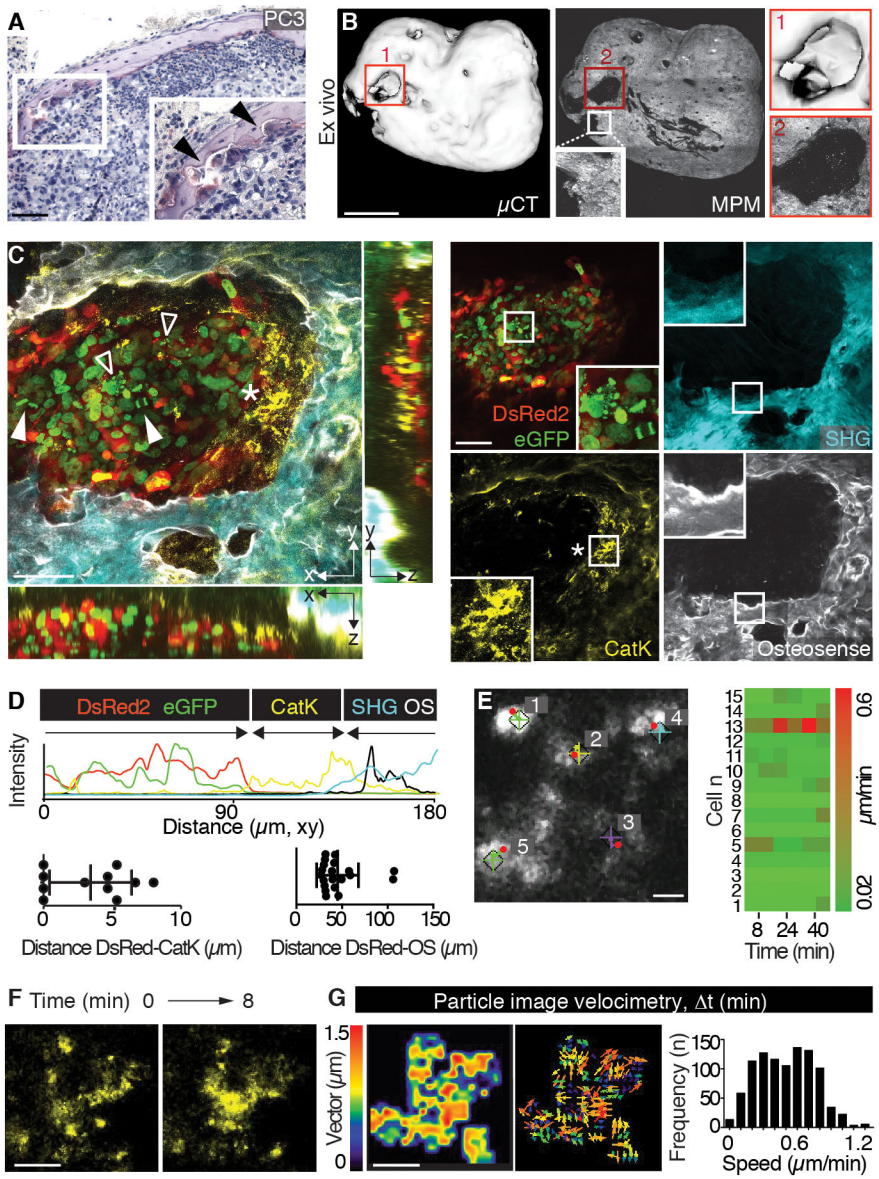

Fig. 4. Monitoring of osteolysis and dynamics of cathepsin K$^+$ cells.

(A) TRAP staining of PC3 lesion in mTEBC. Box, inset (magnification). Arrowheads indicate osteoclasts. Bar, 100 μm. **(B)** Evaluation of osteolysis by ex vivo μCT and SHG detection by MPM. Magnifications of numbered boxed regions are shown. Bar, 1 mm. **(C)** iMPM detection of an osteolytic lesion. Merged xy and xz, yz orthogonal views, single channels and details are shown. Box, magnification. Nucleus = H2B/eGFP, green; cytoplasm = DsRed2, red; collagen fibers, bone = SHG, cyan; bone remodeling = OS, white; osteoclast/phagocyte = cathepsin K (Cat K), yellow. Solid arrowhead, mitotic event; void arrowhead, apoptotic nucleus; asterisk, Cat K$^+$ cells. Bar, 100 μm. **(D)** Imaging analysis, xy intensity profile for single channels and quantification of the distance between tumor border (first layer of cells, DsRed2) and osteoclast/phagocyte (Cat K) or bone (OS). Scatter diagrams represent measurements from different regions in 3 independent lesions. **(E)** Dynamics of Cat K$^+$ events monitored by time-lapse iMPM and analyzed by tracking. "+"

and diamonds indicate the start and red dots the final position of each cell, numbers indicate individual cells. Right panel, heatmap of the speed of 15 representative cells. Bar, 20 μm. (**F, G**) Cat K signal detected over time by time lapse iMPM (**F)** and particle imaging velocimetry (PIV) obtained by whole-field analysis (**G**). Two sequential frames obtained at different time points (0 and 8 min) from movie S2 are shown. Bar, 10 μm. Magnitude, vector map and speed frequency distribution (3–4 areas/tumor, from 3 mice).

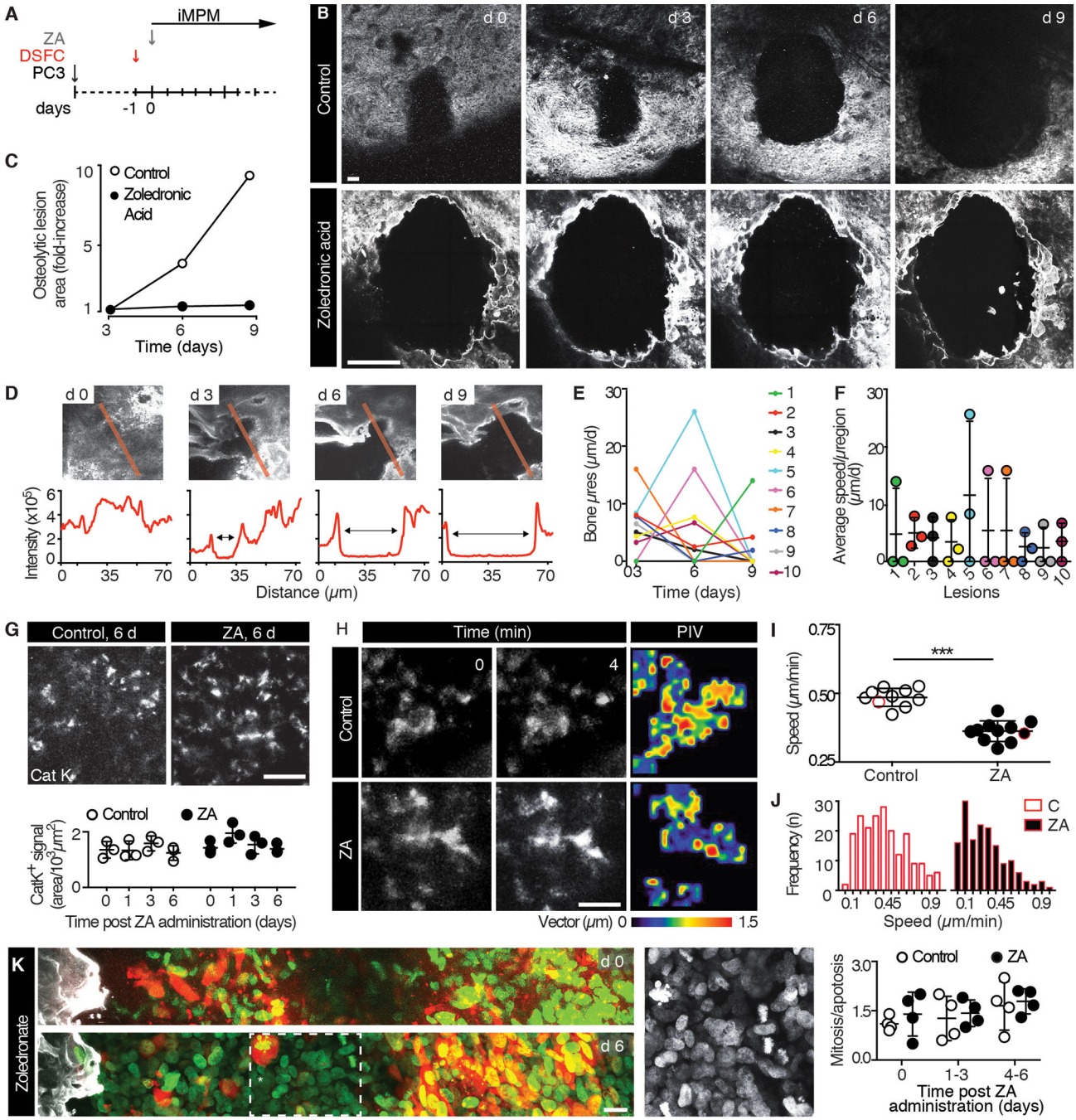

Fig. 5. Response to zoledronic acid therapy monitored by iMPM.

(**A**) Schematic representation of the experimental schedule. 10–14 days after PC3 cells injection, mice were implanted with a DSFC and treated with zoledronic acid (ZA; 20 μg/mouse in saline by a single intravenous injection) the subsequent day. (**B, C**) Longitudinal monitoring of osteolytic progression by SHG detection at iMPM in control (vehicle, saline) and zoledronic acid treated mice and quantification of the resorbed area of lesions represented in (**B**). Bar, 100 μm. Note the different scale of the images representing control and zoledronic acid treated tumors to accommodate the different size of the osteolytic

region. (**D**) Imaging analysis of micro-osteolytic lesion progression in ZA treated mice. (**E, F**) Quantification of the μspeed of bone resorption in individual subregions (**E**) and corresponding average μspeed/subregion over time representing the changes from days 0–9 (**F**). Data show the mean ± SD; n=10 microregions from 3 independent osteolytic lesions. (**G**) Density of Cat K signal over time. Mean ± SD, n=3 independent lesions/time point. Bar, 100 μm. No significant difference was identified by one-way ANOVA followed by Tukey's HSD post-hoc test. (**H**) PIV analysis of Cat K signal in control and ZA treated mice; 2 representative frames and magnitude map. Bar, 20 μm. Area, 65 × 65 μm. (**I, J**) Average speed in control and ZA treated mice. Mean ± SD. For image analysis, the quantification of PIV was obtained from 3–4 areas/lesion, from 4 mice/group. Speed distribution obtained from representative cells highlighted by red-outline in panel (**I**). *** $P<0.001$ by Student t-test, unpaired, two-tailed. (**K**) PC3 cell replicative status. Representative images taken at the onset and 6 d after ZA application (left panels) and quantification of the ratio between mitotic and apoptotic cells at different time points (right diagram); mean ± SD, n=4 independent lesions/time point. Bar, 10 μm. No significant difference was identified by one-way ANOVA followed by Tukey's HSD post-hoc test.